Available online at www.sciencedirect.com
ScienceDirect
International Journal of Heat and Mass Transfer 51 (2008) 2075–2089
International Journal of HEAT and MASS TRANSFER
www.elsevier.com/locate/ijhmt

Laminar heat transfer enhancement downstream of a backward facing step by using a pulsating flow

A. Velazquez [a,*], J.R. Arias [a], B. Mendez [b]

[a] Propulsion and Fluid Mechanics Department, School of Aeronautics, Universidad Politécnica de Madrid, Plaza Cardenal Cisneros 3, 28040 Madrid, Spain
[b] Fluid Mechanics Area, Universidad Carlos III de Madrid, Avenida de la Universidad 30, 28911 Leganés, Madrid, Spain

Received 14 June 2006
Available online 10 August 2007

Abstract

This study is motivated by the need to devise means to enhance heat transfer in configurations, like the back step, that appear in certain types of MEMS that involve fluid flow and that are not very efficient from the thermal transfer point of view. In particular, the work described in this paper studies the effect that a prescribed flow pulsation (defined by two control parameters: velocity pulsation frequency and pressure gradient amplitude at the inlet section) has on the heat transfer rate behind a backward facing step in the unsteady laminar 2-D regime. The working fluid that we have considered is water with temperature dependent viscosity and thermal conductivity. We have found that, for inlet pressure gradients that avoid flow reversal at both the upstream and downstream boundary conditions, the time-averaged Nusselt number behind the step depends on the two above mentioned control parameters and is always larger than in the steady-state case. At Reynolds 100 and pulsating at the resonance frequency, the maximum time-averaged Nusselt number in the horizontal wall region located behind the step whose length is four times the step height is 55% larger than in the steady-case. Away from the resonant pulsation frequency, the time-averaged Nusselt number smoothly decreases and approaches its steady-state value.
© 2007 Elsevier Ltd. All rights reserved.

Keywords: Back; Step; Unsteady; Laminar; Pulsating

1. Introduction

Nowadays, there is a large variety of Micro-Electro-Mechanical systems (MEMS) that, in one way or another, involve fluid flow and heat transfer effects. Practical applications of these systems include, for instance, micro-motors, micro-cooling devices and power-MEMS. When dealing with specific engineering design aspects, it often happens that because of manufacturing restrictions, or the need to keep a low product cost, channel configurations inside this type of MEMS are far from being fully optimised. For example, it is not unusual to find deep recess, sharp bends, grooves, and both forward and backward facing step like structures inside some designs. Since the surface to volume ratio grows when the typical characteristic length of the system diminishes, associated heat losses could become important and corrective actions might be implemented. In some specific cases, heat losses are so critical that new configurations need to be devised to fulfil certain objectives. For instance, micro-combustion based on arrays of catalytic wires is being pursued actively because thermal losses in the micro-scale may prevent combustion to occur in the shape of a conventional stabilised flame.

The objective of this paper is to study the effect that forced flow pulsation may have on laminar heat transfer enhancement behind a 2-D backwards facing step. We have chosen this configuration because it represents a broad class of geometries to be found inside fluid-thermal MEMS. Since we foresee liquid cooling applications, the focus of our study is on the laminar, unsteady, incompressible flow regime. For instance, if we consider a backwards facing step whose inlet channel has an height of 225 μm

* Corresponding author. Tel.: +34 91 336 6351.
E-mail address: avelazquez@aero.upm.es (A. Velazquez).

0017-9310/$ - see front matter © 2007 Elsevier Ltd. All rights reserved.
doi:10.1016/j.ijheatmasstransfer.2007.06.009

Nomenclature

Latin symbols

a_2	control parameter for pressure gradient at inlet section
$c_{p\infty}$	specific heat at inlet section
D_h	hydraulic diameter of the inlet channel
eq_27	acronym for Eq. (27)
Gr	Grashof number
g	gravity constant
h_x	local convection coefficient behind the step
k	dimensionless thermal conductivity
k'	thermal conductivity
k_∞	thermal conductivity at inlet section
Nu_x	local Nusselt number behind the step
n	direction normal to a surface
P	dimensionless pressure
P'	pressure
Pr	Prandtl number
Re	Reynolds number based on D_h and u_∞
$Re_{\delta'}$	Reynolds number based on the Stokes thickness
RHS	acronym for right hand side
t	dimensionless time
t'	time
t^*	dimensionless pseudo-time
T	dimensionless fluid temperature
T'	temperature
T_∞	fluid temperature at inlet section
u	dimensionless horizontal velocity component
u_{max}	maximum centreline velocity in a Poiseuille type solution
u'	horizontal velocity component
u_∞	mean horizontal velocity component at inlet section
v	dimensionless vertical velocity component
v'	vertical velocity component
x	dimensionless horizontal co-ordinate
x'	horizontal co-ordinate
y	dimensionless vertical co-ordinate
y'	vertical co-ordinate

Greek symbols

β	pseudo-compressibility parameter
β_{exp}	thermal expansion coefficient
δ'	stokes layer thickness
Δ	increment
Φ	functional approximation for the Finite Point algorithm
λ_0 to λ_5	parameters that define the functional approximation Φ
μ	dimensionless dynamics viscosity
μ'	dynamic viscosity
μ_∞	dynamic viscosity at inlet section
ν'	kinematic viscosity
ρ_∞	density at inlet section
ω	dimensionless pulsation frequency
ω'	dimensional pulsation frequency

Superscripts

k	time instant
o	initial time in the integration loop

(hydraulic diameter D_h equal to 450 μm), an step height of 225 μm, and water flows in at 293 K and 0.22 m/s, the Reynolds number based on the mean inlet velocity and hydraulic diameter is 100.

Also, we will concentrate on the 2-D regime because the onset of 3-D effects is expected to occur at higher Reynolds numbers. Armaly et al. [1] reported, based on their own experimental data, a critical Reynolds number of 400 for this onset. Durst and Pereira [2] found good agreement between experimental and numerical 2-D results for Reynolds numbers below 648. Kaiktsis et al. [3], by using direct numerical simulation, suggested that the critical Reynolds number is 700. More recently, Barkley et al. [4] have shown, by performing a stability analysis, that the onset of 3-D effects starts a Reynolds 997 (this figure has been corrected to be consistent with the Reynolds number definition used in Refs. [1–3] and in the present study). Barkley et al. [4] have also discussed in detail these discrepancies and concluded that the reason for the rather low critical Reynolds number (400) found by Armaly et al. [1] is the presence of end wall effects. In particular, the span-wise aspect ratio of their experimental set up was 36:1, while Barkley et al. [4] considered an ideal 2-D geometry in their computations. Summarizing, since we will consider Reynolds numbers of the other of 100, we can assume that the hypothesis of two-dimensionality is well satisfied. We also include in our analysis the temperature dependence of both viscosity and thermal conductivity. Water viscosity changes by a factor of three in the temperature span ranging from 293 K to 353 K that we have considered, see Incropera and DeWitt [5], and that is typical of some electronics systems cooling applications. Since flow topology is very sensitive to the Reynolds number in the regime that we consider, see [1,2], we decided to account for real fluid effects from the outset.

The idea of using pulsating flows to enhance laminar heat convection is not new although the outcome of the many studies that have been performed up to now still remains controversial. The situation is best summarised in the introduction of the paper published by Yu et al. [6] where they classify previous work into four categories according to the conclusion being reached:

- Pulsation enhances heat transfer [7].
- Pulsation deteriorates heat transfer [8].
- Pulsation does not affect heat transfer [9].
- Heat transfer enhancement of deterioration may occur depending on the flow parameters [10].

Incidentally, the authors of the review, Yu et al. [6], conclude from their own work that pulsation neither enhances nor deteriorates heat flow. Recently, another study on the subject has been published by Chattopadhyay et al. [11] and they report that pulsation has no effect on the time-averaged heat transfer along straight channels.

Regarding the backward facing step flow under consideration, a comprehensive review of steady heat transfer results has been published by Abu-Malaweh [12] for a wide range of configurations and flow properties. Other recent studies on heat transfer effects on 2-D and 3-D backward facing step geometries have been published by Abu-Hijleh [13], Nie and Armaly [14] and Iwai et al. [15]. In the isothermal case with no heat transfer effects, a detailed analysis that addresses the different flow topologies that appear as a function of the Reynolds number has been reported by Chiang and Sheu [16].

Some aspects of laminar heat transfer downstream of a back-step whit pulsating and non-pulsating inlet conditions have been studied previously by Valencia and Hinojosa [17]. In this paper, the authors dealt with air having constant viscosity and thermal conductivity properties, and assumed a parabolic inlet velocity profile with sinusoidal time variation. For the case of pulsating flow, they considered the case of one Strouhal number and found this specific pulsation enhanced heat transfer by a time-averaged factor of 9% in the lower wall when compared to the steady flow situation. A similar study in the turbulent regime has been reported by Valencia [18]. In this case, the changes in the lower wall Nusselt number caused by pulsating conditions appeared to be smaller than in the laminar case. Anther study on the effect of pulsation on laminar heat transfer has been published by Chang and Tucker [19], where they address the problem of laminar flow around a sharp 180° bend. In order to enhance heat transfer, they placed a thin fin right before the bend so as to achieve a self-sustained oscillatory separated flow region. In their conclusions, they stated that these self-sustained oscillations cause a substantial reduction in reattachment length and, accordingly, a sizable increase in the local Nusselt number. Another reference worth noticing in this context is the study by Yoshioka et al. [20]. In this work, the authors pointed out that the evolution of organised vortex motion behind a back-step in the turbulent regime is strongly dependent on the imposed inlet perturbation.

The work presented in this paper differs from previous ones because of three main aspects: (a) we consider the flow of water having temperature dependent viscosity and thermal conductivity (this is important because water viscosity changes by a factor of 3 in the range from 293 K to 353 K typical of many industrial applications), (b) we specifically search for the pulsation amplitudes and frequencies that maximise heat transfer behind the step and (c) we present the resonant behaviour of the Nusselt number as a function of the pulsation parameters. Concerning the organisation of the work presented hereafter, the chapters that follow are: problem description, governing equations, boundary conditions, spatial and temporal discretisation, validation, results, sensitivity of the results and conclusions.

2. Problem description

We study the effect that forced flow pulsation has on the heat transfer rate behind a backward facing step in the 2-D, laminar incompressible flow regime. The non-dimensional geometry of the problem is shown in Fig. 1. Distances are rendered dimensionless by using the hydraulic diameter of the inlet channel. All walls are adiabatic except a portion of length $L = 5$ on the lowest wall downstream of the step where temperature is prescribed. In this way we isolate the effect that we are looking for, and we do not have interference from thermal effects caused by other walls.

Our cooling fluid is water and we assume that it enters the computational domain at the ambient temperature of 293 K. Wall temperature at the lowest wall downstream of the expansion is 353 K. These two temperatures represent a typical situation found in electronics systems cooling applications. To have a continuous dependence of viscosity and thermal conductivity on temperature, we have interpolated the experimental data provided by Incropera and Dewitt [5]. The functions that we use are:

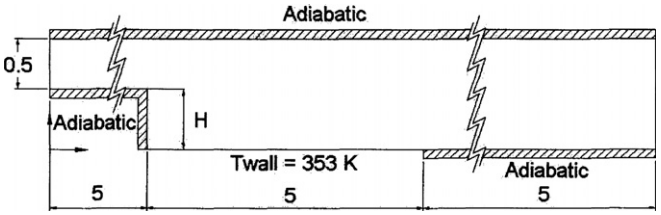

Fig. 1. Problem definition.

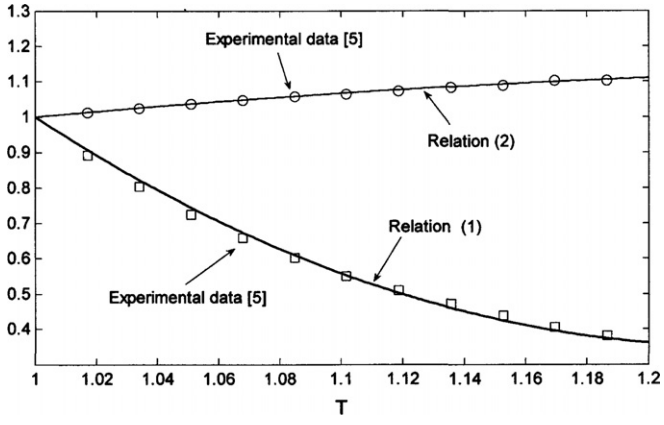

Fig. 2. Comparison between correlations generated for dynamic viscosity and thermal conductivity, and experimental data.

$$\mu = \frac{\mu'}{\mu_{293\,\mathrm{K}}} = 1 - 5.646 \cdot (T-1) + 12.259 \cdot (T-1)^2 \quad (1)$$

$$k = \frac{k'}{k_{293\,\mathrm{K}}} = 1 + 0.786 \cdot (T-1) + 1.176 \cdot (T-1)^2 \quad (2)$$

where μ' and k' are the dimensional dynamic viscosity ant thermal conductivity, respectively. The dimensionless temperature T is obtained by dividing the actual temperature by the reference inlet temperature (293 K). Fig. 2 shows the relations (1) and (2) and their comparison with the experimental data provided in Ref. [5] in the range from 293 K ($T = 1.0$) to 353 K ($T = 1.2$).

3. Governing equations

Dimensionless equations of the problem are continuity, x and y momentum and energy:

$$\frac{\partial u}{\partial x} + \frac{\partial v}{\partial y} = 0 \quad (3)$$

$$\frac{\partial u}{\partial t} + u\frac{\partial u}{\partial x} + v\frac{\partial u}{\partial y} = -\frac{\partial P}{\partial x} + \frac{1}{Re}\left[\mu\left(\frac{\partial^2 u}{\partial x^2} + \frac{\partial^2 v}{\partial y^2}\right) + 2\frac{\partial \mu}{\partial x}\frac{\partial u}{\partial x} + \frac{\partial \mu}{\partial y}\left(\frac{\partial u}{\partial y} + \frac{\partial v}{\partial x}\right)\right] \quad (4)$$

$$\frac{\partial v}{\partial t} + u\frac{\partial v}{\partial x} + v\frac{\partial v}{\partial y} = -\frac{\partial P}{\partial y} + \frac{1}{Re}\left[\mu\left(\frac{\partial^2 v}{\partial x^2} + \frac{\partial^2 v}{\partial y^2}\right) + 2\frac{\partial \mu}{\partial y}\frac{\partial v}{\partial y} + \frac{\partial \mu}{\partial x}\left(\frac{\partial v}{\partial x} + \frac{\partial u}{\partial y}\right)\right] \quad (5)$$

$$\frac{\partial T}{\partial t} + u\frac{\partial T}{\partial x} + v\frac{\partial T}{\partial y} = \frac{1}{RePr}\left[k\left(\frac{\partial^2 T}{\partial x^2} + \frac{\partial^2 T}{\partial x^2}\right) + \frac{\partial k}{\partial x}\frac{\partial T}{\partial x} + \frac{\partial k}{\partial y}\frac{\partial T}{\partial y}\right] \quad (6)$$

Dimensionless variables are defined as follows:

$$u = \frac{u'}{u_\infty}, \quad v = \frac{v'}{v_\infty}, \quad P = \frac{P'}{\rho_\infty u_\infty^2}, \quad T = \frac{T'}{T_\infty} \quad (7)$$

$$x = \frac{x'}{D_\mathrm{h}}, \quad y = \frac{y'}{D_\mathrm{h}}, \quad t = \frac{t' u_\infty}{D_\mathrm{h}} \quad (8)$$

where u, v, P, T, x, y and t stand for horizontal and vertical velocity components, pressure, temperature, horizontal and vertical spatial co-ordinates and temperature, respectively. Dotted variables are dimensional and the subscript ∞ denotes unperturbed values upstream of the inlet. D_h is the hydraulic diameter of the inlet channel. The Reynolds number is defined as

$$Re = \frac{\rho_\infty u_\infty D_\mathrm{h}}{\mu_\infty} \quad (9)$$

Armaly et al. [1] used $(2/3)u_{\max}$ to define the Reynolds number, with $u_{\max}$ being the maximum centreline velocity. Since $u_\infty = (2/3)u_{\max}$ for a Poiseuille type inlet velocity profile, it follows that we use the same definition as they do. Prandtl number Pr $(\mu_\infty c_{p\infty}/k_\infty)$ is also defined by using upstream values. μ and k appearing in Eqs. (4)–(6) are taken from the relations (1) and (2).

In the regime that we consider, flow topology depends strongly on the Reynolds number. For instance, for a step height of 0.5 in steady flow (see Fig. 1), Armaly et al. [1] reported that the reattachment length is 1.44 and 3.23 for Reynolds 100 and 389, respectively. In our case, we have temperature variations of the order of 80 K in the flow field (form 293 K to 353 K) and this causes local viscosity (and local Reynolds number) to change by a factor of the order of 3. Then, we have a strong coupling via temperature of Eqs. (4)–(6). Finally, we have not included the viscous dissipation function in the energy equation because this term is of the order of $u_\infty^2/(Rec_{p_\infty}T_\infty)$, that is negligible in our case compared to the other equation terms.

Regarding the model described by Eqs. (3)–(6), we have made two hypotheses that need to be justified. The first one is to assume laminar behaviour even though the flow has an oscillating nature. The second is related to the fact that buoyancy terms are not included in the momentum equations. Transition of wall-bounded unsteady profiles has been studied, among others, by Das and Arakeri [21], Akhavan et al. [22,23] and Hino et al. [24]. They have provided criteria to ascertain the onset of transition in straight ducts by using the Reynolds number $(Re_{\delta'})$ based on the Stokes layer thickness $\delta' = (2\nu'/\omega')^{1/2}$, where ν' is the fluid kinematic viscosity and ω_0' is the dimensional pulsation frequency. It is to be noted that, as Das and Arakeri [21] remark in page 263 of their work, vortex formation does not always leads to turbulence. In particular, these authors found that no transition to turbulence occurs for $Re_{\delta'} \leqslant 1200$. The criteria provided by Hino et al. [24] is somewhat more restrictive and sets up the transition Reynolds number in the range from 500 to 550. We have, in our case, a sudden expansion so the above mentioned criteria are not directly applicable. However, we could estimate our range of $Re_{\delta'}$ and see how far we stand from those critical values. As it will be mentioned in the next section, we deal with hydraulic diameters and flow velocities of the order of 450 μm and 0.22 m/s, respectively. Also, we find that for these parameters, maximum heat transfer occurs at pulsating frequencies of 537 rad/s (85 Hz) so, in this case, we have $Re_{\delta'} = 22$ that is more than one order of magnitude smaller than the critical values for transition. In line with this reasoning, it is to be noted that in the already mentioned work performed by Valencia and Hinojosa [17] the flow was considered to be laminar as well. Dimensionless buoyancy terms scale as Gr/Re^2 where Gr is the Grashof number. In our case, with inlet channel height in the range from 100 to 200 μm, maximum temperature differences of 60 K, and $Re = 100$, the ratio Gr/Re^2 varies from 1.0e−3 to 1.0e−4, so we have not accounted for this effect (as in Ref. [17]).

4. Boundary conditions

Before writing down the boundary conditions of the problem, we first describe the solution of the unsteady

Poiseuille flow in a 2-D channel. The governing equation of this problem is

$$\frac{\partial u}{\partial t} = -\frac{\partial p}{\partial x} + \frac{1}{Re}\frac{\partial^2 u}{\partial y^2} \tag{10}$$

Solutions are sought as follows:

$$u(y,t) = u_1(y) + u_2(y,t) \tag{11}$$

$$\frac{\partial P}{\partial x} = -a_1 + a_1 a_2 \cos(2\pi\omega t) \tag{12}$$

where ω is the prescribed dimensionless frequency for the pressure gradient and the product $a_1 a_2$ is its amplitude. Solution of system (10)–(12), see [25], is

$$a_1 = \frac{48}{Re} \tag{13}$$

$$u_1(y) = -24\left(y^2 - \frac{y}{2}\right) \tag{14}$$

$$u_2(y,t) = \mathrm{Real}\left[\frac{\mathrm{i}a_1 a_2 \mathrm{e}^{\mathrm{i}2\pi\omega t}}{2\pi\omega}\left(\frac{1}{\alpha+1}\mathrm{e}^{\psi y} + \frac{\alpha}{\alpha+1}\mathrm{e}^{-\psi y} - 1\right)\right] \tag{15}$$

where

$$\psi = (\mathrm{i}2\pi\omega Re)^{1/2} \tag{16}$$

$$\alpha = \mathrm{e}^{\psi/2} \tag{17}$$

Solution ((11) and (12)) is formally valid for a pulsating flow inside an infinitely long 2-D straight channel so it should not be used as the inlet boundary condition in our back step problem. What we do is to retain the velocity profile (11) and the control parameters ω (frequency) and a_2 (amplitude) that define the pulsating flow, and relax the pressure boundary condition so that it adapts itself to both the velocity pulsation and back step geometry. Accordingly, our boundary conditions are:

- Inlet

  $$u(y,t) = u_1(y) + u_2(y,t) \tag{11}$$

  where $u_1(y)$ and $u_2(y,t)$ are defined by relations (14)–(17).

  $$v = 0 \tag{18}$$

  $$\frac{\partial^2 P}{\partial x^2} = 0 \tag{19}$$

  $$T = 1 \tag{20}$$

  Boundary condition (19) allows for a self-adapting time variation of the pressure gradient at the inlet. Boundary condition (20) assumes an isothermal incoming flow that is consistent with Eqs. (3)–(6) and with the fact that the inlet channel walls are adiabatic.Boundary condition (11) pulsates, see relation (15), with the argument $2\pi\omega t$. According to our definition of the dimensionless variables, this argument is equal to $2\pi\omega t' u_\infty / D_h$, where t' is the dimensional time measured in seconds. If we select a typical case, like the one mentioned in the introduction with $D_h = 450$ microns and $u_\infty = 0.22$ m/s, and prescribe $\omega = 0.1$ (as we will show later, relevant heat transfer enhancement occurs in the range $\omega = 0.1$ to $\omega = 0.2$ for Reynolds 100) the time needed to complete a full pulsating cycle is 0.02 s (50 Hz). That is, an experiment could be realised by using an off-the-shelf reciprocating pump that oscillates at the grid frequency (50 Hz), together with a frequency adaptor to sweep for different values of ω.
- Outlet

  $$\frac{\partial u}{\partial x} = \frac{\partial v}{\partial x} = \frac{\partial^2 P}{\partial x^2} = \frac{\partial T}{\partial x} = 0 \tag{21}$$

  The formulation of outflow boundary conditions for the incompressible Navier–Stokes equations when computing either external or internal flows is still a subject of active research; see, for example, the work reported by Olshanskii and Staroverov [26], Hasan et al. [27] and Nordstrom et al. [28]. We have used, in the present work, the approximate boundary conditions (21) that assume that the flow is fully developed at the outlet section. These conditions, that are admissible provided that the outlet boundary is located far enough downstream, have also been used by many researchers dealing with internal unsteady flows. Three practical application cases are, for example, those presented by Valencia and Hinojosa [17], Kaiktsis et al. [29] and Wang and Zhang [30]. Other approaches consist, for instance, on the use of the so called "traction free" conditions, Wang and Sheu [31], or setting to zero all second order derivatives of the primitive variables, Chattopadhyay et al. [11]. In any case, in the last section of this paper (sensitivity of the results) we present some additional results obtained by using a longer computational domain so as to check that the outflow boundary condition (21) does not influence the computed parameters.
- Solid walls

  $$u = v = 0 \tag{22}$$

  $$T = T_{\mathrm{wall}} \quad \text{for } 5 \leqslant x \leqslant 10, \quad y = 0 \tag{23}$$

  $$\frac{\partial T}{\partial n} = 0 \quad \text{for any other wall} \tag{24}$$

  Pressure boundary condition at vertical or horizontal walls is obtained by computing the momentum equations (4) or (5) with zero velocity and one-sided (into the flow domain) derivatives. Pressure at the two corners of co-ordinates (5, 0.5) and (5, 0), is obtained by combining and solving Eqs. (4) and (5) along the direction that bisects the corners (45° in our case).

5. Spatial and temporal discretisation

Regarding spatial discretisation, we use the Finite Point formulation developed by Mendez and Velazquez [32,33] whose main features are:

- Spatial derivatives are computed by using a least squares approximation in a cloud of points.
- Second order Taylor polynomials are used as the approximating functions

$$\Phi(x,y) = \lambda_0 + \lambda_1 x + \lambda_2 y + \lambda_3 x^2 + \lambda_4 y^2 + \lambda_5 xy \tag{25}$$

  where Φ stands for any flow variable and the λ_i's are computed in a least squares sense.
- Each cloud contains seven points (a central point plus six neighbours). The closest point to the centrum maps the 2-D space into four different sectors that span 90° each, see Fig. 3. The first four neighbours are taken from each of the four sectors by choosing the closest point to the central one. The fifth and sixth points are chosen at random from two of the sectors so that computation of the spatial derivatives does not favour any particular direction in the x–y plane.

We use a Cartesian grid in the work described in this paper, so we could have chosen a far simpler centred finite difference numerical algorithm. However, since we have future applications in mind where the implementation of Cartesian grids is no longer possible, we decided to use a Finite Point scheme from the outset. These schemes are attractive for practical industrial applications because they are very flexible from the geometry modellisation point of view and, also, because they are well suited to deal with moving surfaces. The reason is that clouds of points may penetrate each other without the compatibility constrains required by either finite element or finite volume schemes.

The solver has been extensively validated for different configurations (circular and square cylinders at an angle of attack, and steady-state back steps) for different Reynolds numbers in the vortex shedding laminar regime. In particular, we compared our computed global flow parameters (drag, lift and Strouhal number) with those reported in the literature [32]. Also, we performed a dedicated experimental campaign in a low Reynolds number wind tunnel to validate solver results with regard to time-averaged local flow variables (velocity profiles) and rms values in the unsteady wake behind a square cylinder [33].

Regarding the time integration that we use in the present work, we deviate from the one reported in [32,33]. We have now used the standard implicit pseudo-compressibility approach as described by Tannehil [34], instead of the explicit relaxation-based pseudo-compressibility formulation developed in [32,33]. The reason is that the strong unsteady effects that are felt all over the computational domain in the case of a pulsating internal flow are computed more accurately by using an implicit time integration scheme. Some examples of the practical application of this method have been published by Kiris and Kwak [35].

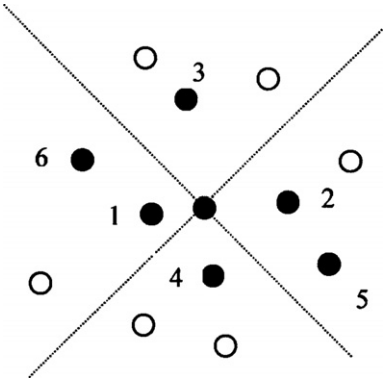

Fig. 3. Set-up of a typical cloud of points.

In particular, the equations that we integrate are:

$$\frac{\partial P}{\partial t^*} + \beta\left(\frac{\partial u}{\partial x} + \frac{\partial v}{\partial y}\right) = 0 \tag{26}$$

$$\frac{\partial u}{\partial t^*} + \frac{\partial u}{\partial t} + u\frac{\partial u}{\partial x} + v\frac{\partial u}{\partial y} = -\frac{\partial P}{\partial x} + \frac{1}{Re}\left[\mu\left(\frac{\partial^2 u}{\partial x^2} + \frac{\partial^2 v}{\partial y^2}\right) + 2\frac{\partial \mu}{\partial x}\frac{\partial u}{\partial x} + \frac{\partial \mu}{\partial x} + \frac{\partial \mu}{\partial y}\left(\frac{\partial u}{\partial y} + \frac{\partial v}{\partial x}\right)\right] \tag{27}$$

$$\frac{\partial v}{\partial t^*} + \frac{\partial v}{\partial t} + u\frac{\partial v}{\partial x} + v\frac{\partial v}{\partial y} = -\frac{\partial P}{\partial y} + \frac{1}{Re}\left[\mu\left(\frac{\partial^2 v}{\partial x^2} + \frac{\partial^2 v}{\partial y^2}\right) + 2\frac{\partial \mu}{\partial y}\frac{\partial v}{\partial y} + \frac{\partial \mu}{\partial x}\left(\frac{\partial v}{\partial x} + \frac{\partial u}{\partial y}\right)\right] \tag{28}$$

$$\frac{\partial T}{\partial t^*} + \frac{\partial T}{\partial t} + u\frac{\partial T}{\partial x} + v\frac{\partial T}{\partial y} = \frac{1}{RePr}\left[k\left(\frac{\partial^2 T}{\partial x^2} + \frac{\partial^2 T}{\partial y^2}\right) + \frac{\partial k}{\partial x}\frac{\partial T}{\partial x} + \frac{\partial k}{\partial y}\frac{\partial T}{\partial y}\right] \tag{29}$$

where β is the pseudo-compressibility parameter that we take it to be 200, see [32,33,35,36]. For each physical time step Δt, Eqs. (26)–(29) are iterated in pseudo-time Δt^* until $|\partial P/\partial t^*|, |\partial u/\partial t^*|, |\partial v/\partial t^*|$ and $|\partial T/\partial t^*|$ are smaller that a certain prescribed value, thereby reverting to the solution of the original set of Eqs. (3)–(6).

Integration in pseudo-time is carried out by using a second order Crank–Nicholson scheme. For instance, if Eq. (27) is re-written in symbolic form as

$$\frac{\partial u}{\partial t^*} + \frac{\partial u}{\partial t} = \{\text{RHS\_eq27}\} \tag{30}$$

where RHS_eq27 stands for the right hand side of Eq. (27), the time integration procedure at each point is formulated as follows:

$$\frac{u^{k+1} - u^k}{\Delta t^*} + \frac{u^k - u^o}{\Delta t} = \frac{1}{2}\left[\{\text{RHS\_eq27}\}^k + \{\text{RHS\_eq27}\}^o\right] \tag{31}$$

where superscript o marks the initial time in the pseudo-time integration loop, and superscript k denotes the intermediate pseudo-time instants. Values of the physical Δt and pseudo-time Δt^* increments, for a given grid and flow parameters, are chosen following the guidelines of the stability analysis performed by Peyret [36].

Keeping in mind the future applications that we have already referred to, we have implemented artificial

dissipation terms in our numerical scheme. In particular, both second and fourth order terms have been used in the continuity equation (26), and fourth order terms in the momentum and energy equations (27)–(29). The implementation of these terms effectively changes the order of the equations (they cause them to become fourth order), so higher order boundary conditions are implemented for the artificial dissipation terms. This specific computational aspect is described in Refs. [32,33].

6. Validation of the numerical algorithm

We have used the experimental results provided by Armaly et al. [1] to validate our solver both at the local and global levels in the adiabatic case. In particular, we computed the steady-state reattachment bubble length behind the step for Reynolds 100 and 389, and found it to be 1.40 and 3.05, respectively. Armaly et al. [1] reported experimental values of 1.44 and 3.23, so our deviations are in the range of 2–5%. Our Cartesian grid contained 32,051 points with a spacing of $\Delta x = \Delta y = 0.2$, so it is to be expected that deviations between numerical and experimental results grow along with the Reynolds number. The computational and physical parameters that we used were: $\Delta t^* = 2.5\text{e}{-4}$, $\Delta t = 2.5\text{e}{-4}$, $\beta = 200$, and $Pr = 6.62$. The fact that walls were kept adiabatic effectively decoupled the energy equation from the others, although we computed it so as to keep the same numerical scheme. Regarding local values of the variables, Fig. 4 shows the comparison between computed and measured [1] local velocity profiles at two sections downstream of the step for the two above mentioned Reynolds numbers.

7. Sensitivity of the results with regard to the computational parameters

In this section, we address the sensitivity of the results obtained with regard to (a) spatial discretisation, (b) temporal discretisation, (c) pseudo-compressibility parameter and (d) length of the computational domain. To address aspects (a)–(c), we have carried out a series of computations (defined in Table 1) for a baseline unsteady case with $\omega = 0.40$ and $a_2 = 1.50$ that is a critical one from the numerical stability point of view since it has a large pulsation frequency and a large pressure gradient parameter. To assess the sensitivity we have chosen three figures of merit: the time-averaged Nusselt number in the region $5 \leqslant x \leqslant 7$ (see Figs. 1 and 5), the maximum local Nusselt number in the same region, and the minimum reattachment length of the recirculation region behind the step along the pulsating cycle. The first two parameters are related to the energy equation while the third concerns the flow topology.

For all cases, step height H was taken to be 0.5, and Prandtl and mean Reynolds number at the inlet section 6.62 and 100, respectively. Water was flowing in at 293 K and wall temperature at the horizontal portion downstream of the step (see Fig. 1) was 353 K ($T = 1.2$). The definition of the local time-dependent Nusselt number Nu_x is as follows:

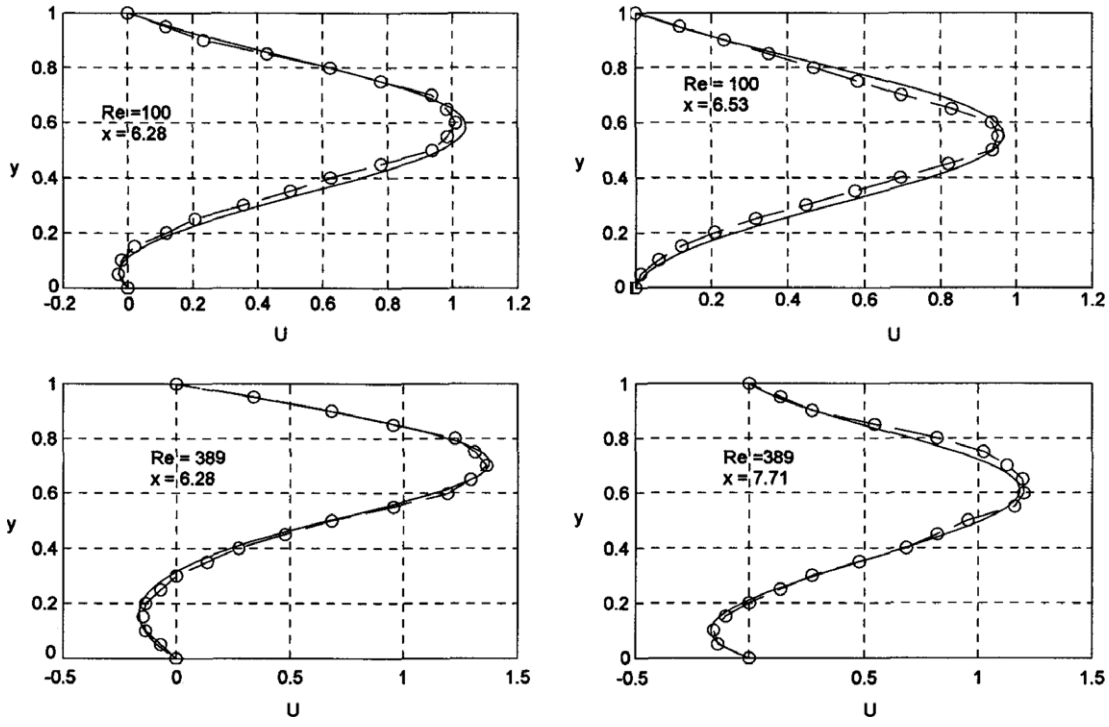

Fig. 4. Comparison between computed (–) and experimental (-○-) local velocity profiles at Reynolds 100 and 389 at different sections downstream of the step.

Table 1
Cases computed to analyze sensitivity of results

Parameters	Case key						
	I	II	III	IV	V	VI	VII
ω	0.40	0.40	0.40	0.40	0.40	0.40	0.40
a_2	1.50	1.50	1.50	1.50	1.50	1.50	1.50
$\Delta x, \Delta y$	2.0e−2	3.3e−2	1.2e−2	2.0e−2	2.0e−2	2.0e−2	2.0e−2
Points in the domain	32,051	11,731	81,281	32,051	32,051	32,051	32,051
$\Delta t, \Delta t^*$	2.5e−4	2.5e−4	2.5e−4	1.2e−4	6.2e−5	2.5e−4	2.5e−4
β	200	100	200	200	200	100	150
Average Nusselt $5 \leqslant x \leqslant 7$	7.48	6.98	7.50	7.41	7.38	7.58	7.52
Maximum local Nusselt	11.02	10.00	11.16	10.96	10.92	11.29	11.11
Minimum reattachment length	1.34	1.30	1.33	1.34	1.34	1.32	1.34

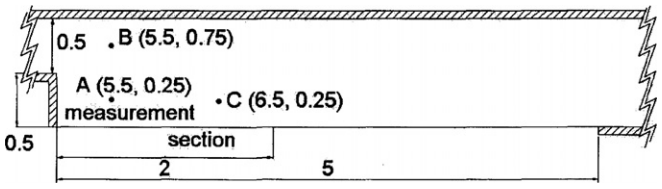

Fig. 5. Location of points A, B and C inside the computational domain.

$$Nu_x(t) = \frac{h_x(t) D_h}{k_{wall}} \tag{32}$$

where $h_x(t)$ is local convection coefficient. Since $\Delta x = \Delta y$ in our Cartesian grid, the local Nusselt number could be written as

$$Nu_x(t) = \frac{D_h}{\Delta y'} \frac{T'_{wall} - T'_{wall+1}(t')}{T'_{wall} - T'_{\infty}} = \frac{1}{\Delta y} \frac{T_{wall} - T_{wall+1}(t)}{T_{wall} - 1} \tag{33}$$

where $T_{wall+1}(t)$ stands for the dimensionless temperature at the grid point located next to the wall along the normal direction. The time-averaged Nusselt number, see relation (34) was computed in a region of length 2 right behind the step, see Fig. 5. The reason for this choice is that, for this step height and Reynolds number, the re-circulating region length in the adiabatic steady-state case is 1.40 so, in this way, we cover the recirculation bubble length.

$$Nu_{average} = \int_{t=0}^{t=t_c} \left(\frac{1}{2} \int_{x=5}^{x=7} Nu_x \, dx \right) dt \tag{34}$$

where t_c is the dimensionless time associated with a full pulsating cycle.

Regarding spatial discretisation, we have generated three computational domains. The baseline case I had 32,051 points with $\Delta x = \Delta y = 0.02$, while case II had 11,731 points and $\Delta x = \Delta y = 0.03333$, and case III was modelled with 81,281 points and $\Delta x = \Delta y = 0.0125$. It was not possible to compute case II with the same pseudo-compressibility parameter $\beta = 200$ of cases I and III. The reason is that the larger values of Δx and Δy did not allow it because of numerical stability reasons. Nevertheless, the results given in Table 1 show that changing Δx and Δy from 3.33e−2 to 2.00e−2 and to 1.25e−2 caused the time-averaged Nusselt number to vary from 6.98 to 7.48 and 7.50, respectively. That is, successive variations of 40% and 38% in Δx and Δy generated successive changes in the time-averaged Nusselt number of 7% and 0.3%, respectively. Similar results are observed for the maximum local Nusselt number and the minimum recirculation region reattachment length, so we could conclude that the results were converged with regard to the spatial discretisation.

Concerning time discretisation, we computed cases IV and V with $\Delta t = \Delta t^* = 1.25e-4$ and $\Delta t = \Delta t^* = 6.25e-5$, while the baseline case I had $\Delta t = \Delta t^* = 2.50e-4$. That is, see Table 1, dividing the time steps by a factor of 2 and 4 caused the time-averaged Nusselt number to change from 7.48 to 7.41 and 7.38, respectively. That is, deviations in the computed result were 0.8% and 0.4%, respectively. Since a similar trend was observed regarding the maximum local Nusselt number and the minimum reattachment length, we could conclude that the results were also converged with regard to the time discretisation. Finally we carried out the same baseline computation ($\beta = 200$) with $\beta = 150$ (case VII) and $\beta = 100$ (case VI). In this case, variations in the time-averaged Nusselt number (7.58–7.52 and to 7.48) were of the order of 0.8% and 0.4%, respectively. A similar behaviour was observed for the other two figures of merit and, accordingly, we could say that the results are also converged with regard to the pseudo-compressibility parameter β.

Aspect (d): length of the computational domain, is related to the justification of the approximate boundary conditions (21) at the outlet section. In all computations presented so far, the outflow section is located 10 dimensionless units downstream of the step that has a non-dimensional height of 0.5 (aspect ratio equal to 20). We have now performed an additional computation of another baseline case with $\omega = 0.15$ and $a_2 = 1.50$ by enlarging the computational domain by an extra 5 dimensionless units (aspect ratio equal to 30) and keeping all other computational parameters unchanged. In this case, the number of points that we used was 44,801. It is to be noted that the aspect ratio used in the work by Valencia and Hinojosa [17] was 10. We have chosen these pulsation parameters

because, as it will be shown in the next section, they provide maximum heat transfer enhancement. The maximum local Nusselt number that we have computed by using the longer domain was 16.56, while we obtained 16.42 with the standard domain. Regarding the space and time-averaged Nusselt number, we have now obtained the value of 8.36 while we computed 8.41 in the baseline case. That is, differences were always less than 1%.

8. Results

We have computed a series of cases with different values of the dimensionless forcing frequency ω and pressure gradient amplitude parameter a_2 at the inlet section. Step height H, and inlet Prandtl and Reynolds numbers were 0.5, 6.62 and 100, respectively. Definition of the computed cases is shown in Table 2, where the minimum and maximum y-averaged inlet Reynolds number is given to provide an idea of the amplitude of the mass flow variation. Again, as in the previous section, water was flowing in at 293 K and wall temperature downstream of the step was 353 K ($T = 1.2$). The results obtained are shown in Fig. 6. Three curves are presented in the upper sub-plot that correspond to different values of parameter a_2 that controls the amplitude of the pressure gradient at the inlet (see Table 2). Frequency of the pulsation is given in the x-axis while the space–time-averaged Nusselt number is presented in the y-axis. The distinctive feature that could be observed is that there is an enhancement of the heat transfer rate in the vicinity of the frequency $\omega = 0.15$. Away from this resonant frequency, the average Nusselt number decreases both in the direction of lower and higher frequencies. The steady-state result ($\omega = 0.0$) is also presented for the sake of completion. The curves move up in the direction of higher heat transfer rates for larger values of the inlet pressure gradient parameter. In the case $\omega = 0.15$ and $a_2 = 1.5$, the Nusselt number (8.41) that is 44% higher than the in the steady case (5.83).

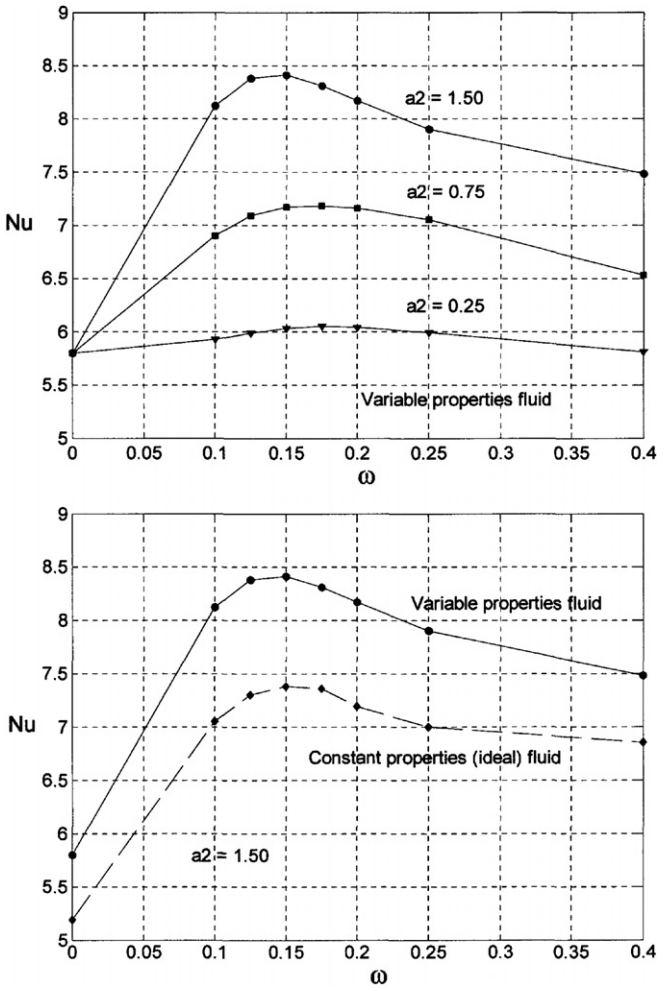

Fig. 6. Upper sub-plot: computed time-averaged Nusselt number versus pulsating frequency for three different values of the a_2 parameter in the variable properties fluid hypothesis. Lower sub-plot: comparison between results obtained by assuming variable and constant fluid properties for the case $a_2 = 1.5$.

Table 2
Definition of computational cases

Case key	ω	a_2	δ	Re_{min}	Re_{max}
01	0.000	0.000	0.000	100	100
11	0.100	0.250	0.251	87	113
12	0.125	0.250	0.251	89	111
13	0.150	0.250	0.252	90	110
14	0.175	0.250	0.252	91	109
15	0.200	0.250	0.251	92	108
16	0.250	0.250	0.252	94	106
17	0.400	0.250	0.251	96	104
21	0.100	0.750	0.752	60	140
22	0.125	0.750	0.752	66	134
23	0.150	0.750	0.754	71	129
24	0.175	0.750	0.753	75	125
25	0.200	0.750	0.753	77	123
26	0.250	0.750	0.752	81	119
27	0.400	0.750	0.751	88	112
31	0.100	1.500	1.503	20	180
32	0.125	1.500	1.505	32	168
33	0.150	1.500	1.512	42	158
34	0.175	1.500	1.510	49	151
35	0.200	1.500	1.507	54	146
36	0.250	1.500	1.509	63	137
37	0.400	1.500	1.510	76	124
41	0.150	2.300	2.318	10	190

The lower sub-plot of Fig. 6 shows, for the case $a_2 = 1.5$, the results obtained by assuming that water is an ideal fluid with constant viscosity and thermal conductivity. Comparison with the results obtained after the variable properties assumption is also given in the same sub-plot. The differences are of the order of 15% in the region where Nusselt number resonance is maxima (co in the range from 0.1 to 0.2). We think that the reason is that water viscosity decreases markedly when the temperature goes up and, therefore, the local Reynolds number in the vicinity of the heated wall is larger than in the ideal case.

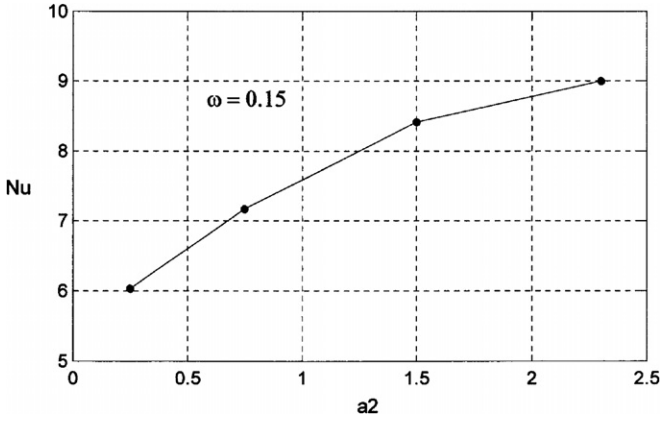

Fig. 7. Computed time-averaged Nusselt number versus a_2 for the pulsating frequency $\omega = 0.15$.

The behaviour shown in both sub-plots of Fig. 6 resembles the typical response of a resonating dynamical system to an externally applied oscillating force. Fig. 7 shows the Nusselt number as a function of the inlet pressure gradient for the resonating frequency $\omega = 0.15$. There, it could be observed that the heat transfer rate does not grow linearly along with the a_2 parameter; i.e.: the second derivative of response amplitude is negative with regard to the amplitude of the forcing parameter, like in the case of a many damped resonating dynamical systems.

For all computation cases presented in Table 2, the time-dependent mass flow was monitored at 10 different vertical sections located inside the computational domain and the variations between each other were found to be less than 1%. Also, for each case, we monitored the time evolution of the inlet pressure gradient, assumed a behaviour of the type stated in relation (12), and computed an equivalent a_2 parameter that we have called δ. This parameter δ is also given in Table 1 where it could be seen that its difference with a_2 is always smaller than 1%. This means that the inlet boundary condition that we use resembles very closely the ideal unsteady Poiseuille solution for a straight channel.

The behaviour presented in Figs. 6 and 7 suggests the existence of a non-linear coupling of resonant nature between thermal effects and Fluid Dynamics parameters. This fact may allow for the application of some kind of flow control, with frequency and amplitude of the inlet pressure gradient acting as the control parameters. Even though the Nusselt number enhancement (55%) in the region right behind the step is not very large, this result suggests that it may be possible to look for resonances in problems that involve large recirculation regions with the objective of improving, among others, the heat transfer rate.

When looking at the results, one of the questions that arise is whether different frequencies appear in the flow field. In this regard, we have checked the time history of all computed results and found no evidence of the existence of frequencies other than the pulsating frequency. Fig. 8 shows the time evolution of u and v along a cycle at points

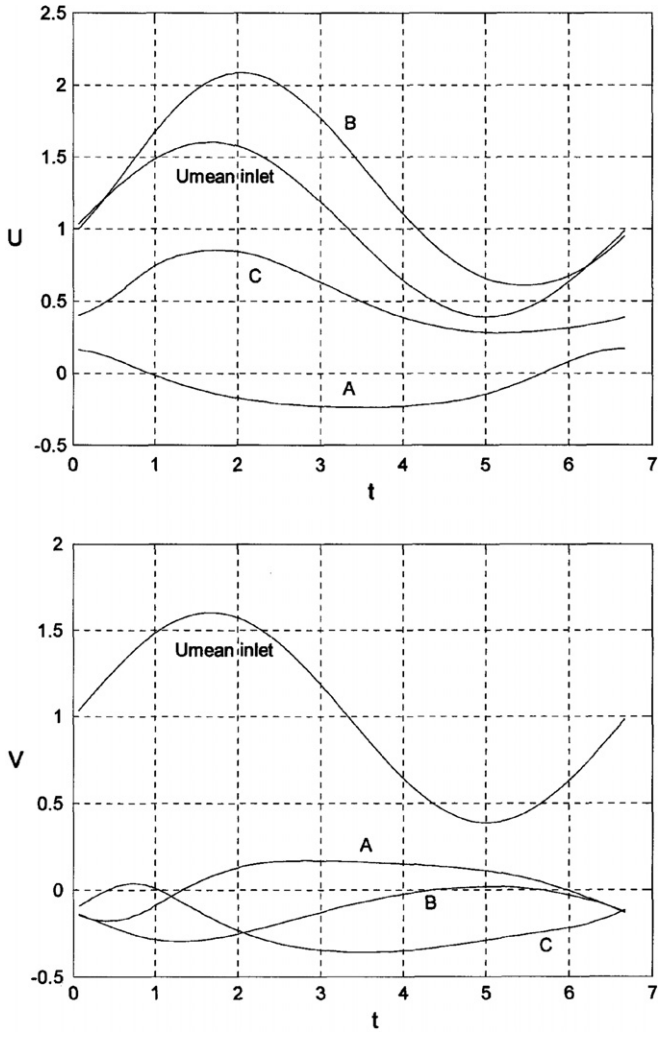

Fig. 8. Time evolution of u and v at points A, B and C for case 33.

A (5.5, 0.25), B (5.5, 0.75) and C (6.5, 0.25), see Fig. 5, for case 33, see Table 2, with $\omega = 0.15$ and $a_2 = 1.5$. The evolution of the average velocity at the inlet section is also shown for reference purposes in the figure. In this case, the dimensionless time needed to complete a pulsating cycle is $1/\omega = 1/0.15 = 6.67$. Two features could be observed in Fig. 8: (a) velocity profiles repeat themselves at the end of the cycle, and (b) outside the recirculation region (point A), horizontal velocity profiles (points B and C) follow qualitatively the pattern of the inlet profile.

The difference between pressure at points A, B and C, and the average inlet pressure is shown in the upper part of Fig. 9. The y-averaged inlet pressure gradient is also shown in the figure as a frame of reference. Again, pressure profiles repeat themselves at the end of the cycle and pressure follows qualitatively the pattern set up in the pulsation. Finally, temperature evolution at the same points A, B and C, is given in the lower plot of Fig. 9. In this case, it is not straightforward to draw a relation with the inlet velocity profile. In fact, the highest temperature at point A, that is representative of the region closest to the step,

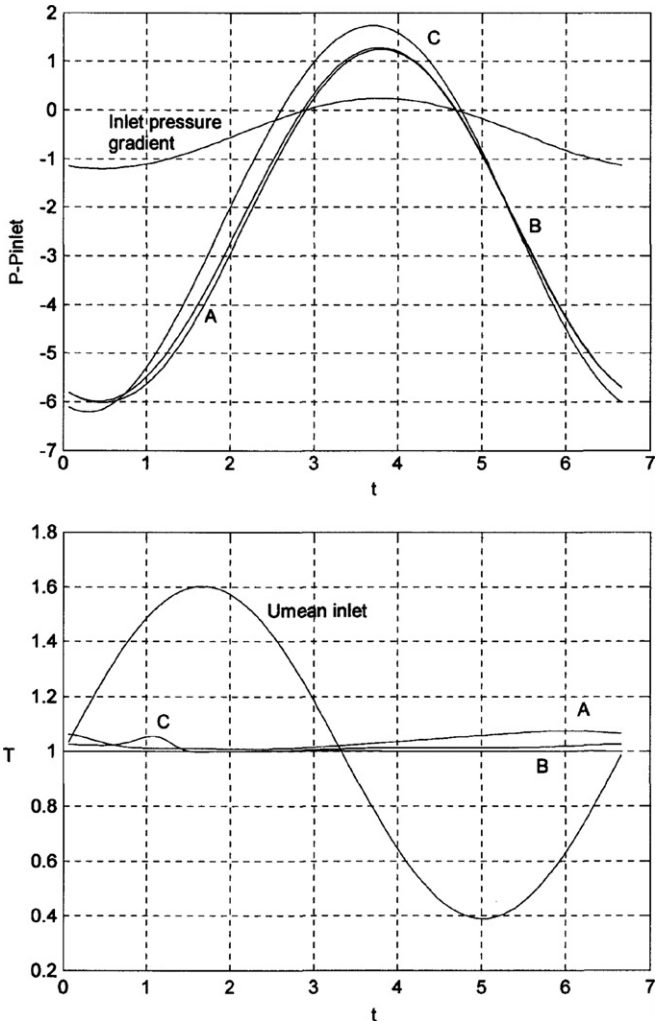

Fig. 9. Time evolution of P and T at points A, B and C for case 33.

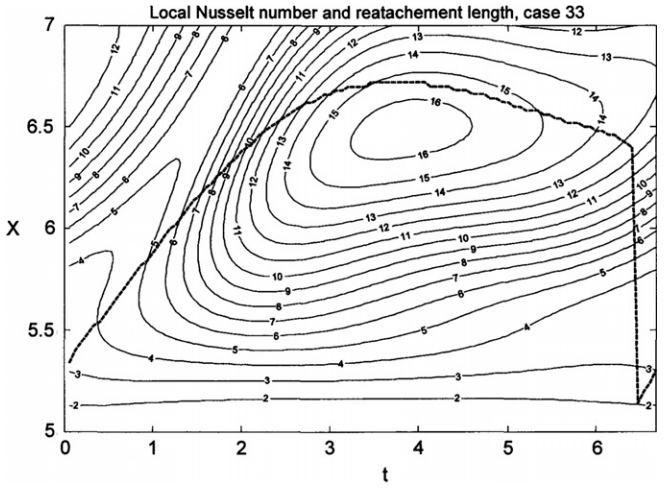

Fig. 10. Local Nusselt number iso-contours behind the step as a function of the x co-ordinate and time along a cycle for case 33. The dashed (– – –) line represents the recirculation region reattachment point as a function of time.

is obtained towards the end of the cycle where inlet velocity is smallest.

An overview of the local Nusselt number in the region $(5 \leqslant x \leqslant 7)$ right behind the step as a function of the dimensionless time $(0 \leqslant t \leqslant 6.67)$ along the pulsating cycle (case 33) is presented in Fig. 10. The Nusselt number in the region very close to the step is low and nearly insensitive to pulsation $(5 \leqslant x \leqslant 5.3, Nu \leqslant 3, \forall t)$. However, further downstream, for instance at $x = 6.5$, the local Nusselt number changes down from 5 up to 16 depending on the time instant. The reattachment point of the recirculation region is also presented in this Fig. 10. It could be observed that the region of the maximum local Nusselt number roughly follows the position of the reattachment point. It is worth to notice, see Figs. 8–10, that the highest values $(Nu \geqslant 14)$ are obtained when the inlet pressure gradient is positive and velocity is minimum. On the contrary, the Nusselt number is minimum $(Nu \sim 5)$ when the inlet pressure gradient is most favourable, and inlet velocity is near its maximum $(1 \leqslant t \leqslant 2)$. This fact suggests that the maximum heat transfer rate is reached out of phase (approximately half a cycle away) from the inlet conditions of largest velocity and most favourable pressure gradient.

We think that the variation of the heat transfer rate is connected to the changes in flow topology along the cycle. Fig. 11 shows 10 equally spaced snapshots of the flow streamlines for the same case 33 and a full pulsating cycle. Time reads top-bottom left–right in Fig. 11. It is to be noted that, in this case, up to four recirculation regions appear in the flow field. In particular, a very large recirculation region appears (and disappears) in the upper wall for snapshots 7 and 8 ($t = 4$ and $t = 5$). The maximum size of this region is 2.06 $(6.28 \leqslant x \leqslant 8.34)$ that is even larger than the recirculation region located right behind the step, and its presence coincides with the time span when the local Nusselt number reaches its maximum (see Fig. 10). This behaviour could be explained by the fact that, in this time span and because of the large size of the upper wall recirculation bubble, deflection of the streamlines is largest when they impinge the lower wall. That is, pulsation generates flow obstacles, large-size low-velocity regions that appear and disappear periodically, that contribute to modify the streamlines pattern and the heat transfer rate. Another approach to enhance mixing is, of course, to manufacture grooves or other obstacles in the channels walls, and this has been the subject of some recent studies [37–39]. Since manufacturing of micro-structures in channels walls might be costly, flow pulsation could be considered as a potential candidate to generate fluid obstacles that may enhance local mixing.

For a given pulsation frequency, the number and extent of recirculation regions decreases for smaller values of the a_2 parameter. Fig. 12 shows, as in Fig. 11, 10 snapshots of case 23 (see Table 2) with $\omega = 0.15$ and $a_2 = 0.75$. Now, the maximum number of recirculation regions is three and their size is much smaller than in the previous case.

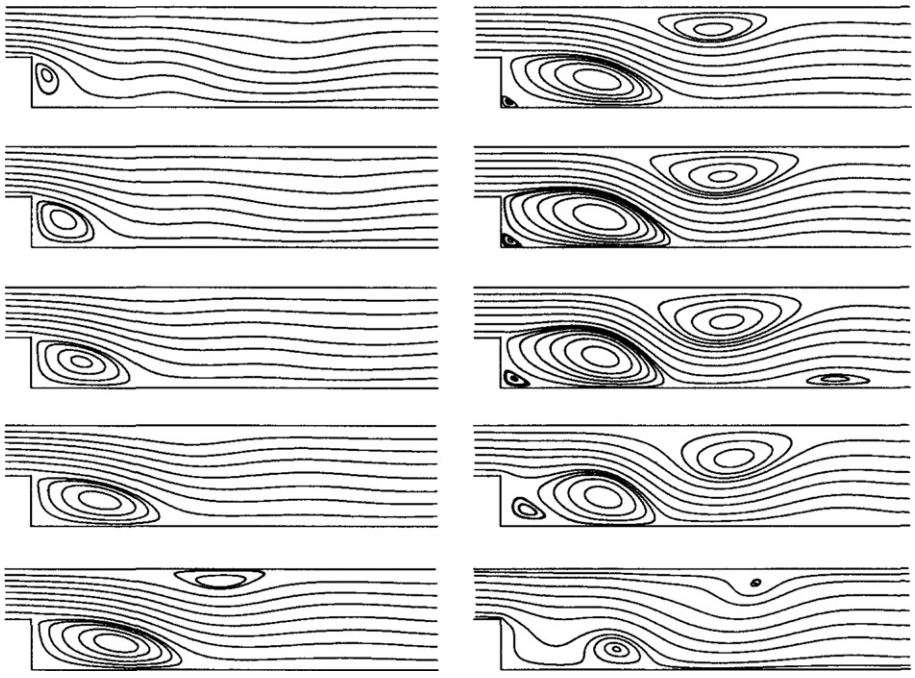

Fig. 11. Snapshots of the streamlines for case 33 along a pulsating cycle. Time reads top-bottom left-right. Snapshots are equally spaced in time.

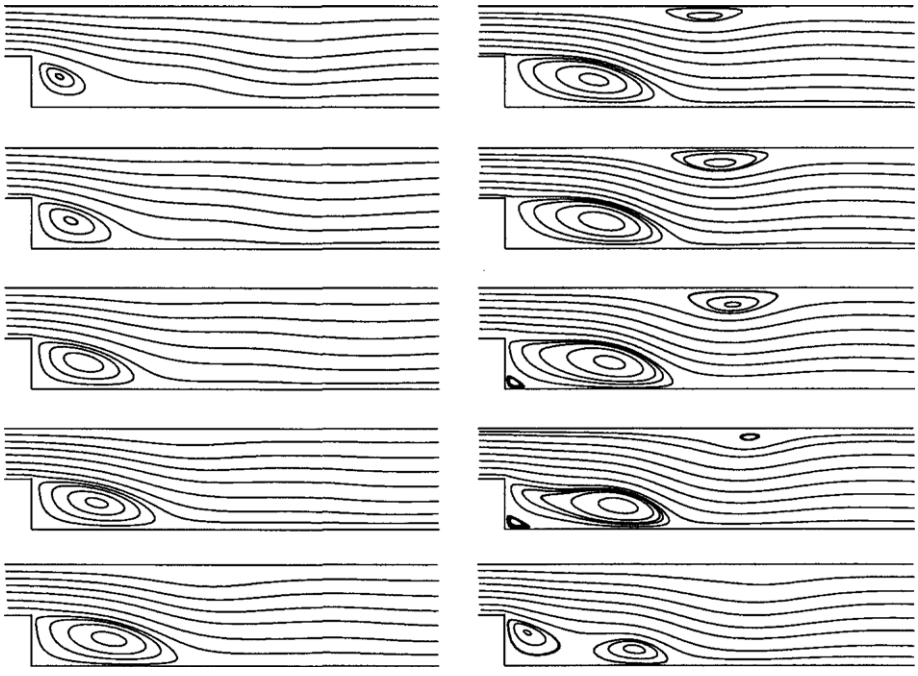

Fig. 12. Snapshots of the streamlines for case 23 along a pulsating cycle. Time reads top-bottom left-right. Snapshots are equally spaced in time.

Fig. 13 presents the time evolution of flow topology for case 13 (see Table 2) with $\omega = 0.15$ and $a_2 = 0.25$ and, in this case, only one slowly contracting and expanding recirculation region is present. Snapshots of case 37 (see Table 2) with $\omega = 0.4$ and $a_2 = 1.5$ are presented in Fig. 14. These results, that should be compared to those presented in Fig. 11 show that increasing frequency from 0.15 (the resonant one) to 0.4 while keeping a_2 constant causes the flow field to exhibit a simpler structure. In this case, only two recirculation regions are present and the one appearing in the upper wall is much smaller than the one that is generated during the resonant pulsation (case 33). As a summary, it could be said that the two control parameters ω and a_2 exert a large influence on the topology of the flow field and that, in turn, this topology controls the heat transfer rate behind the step.

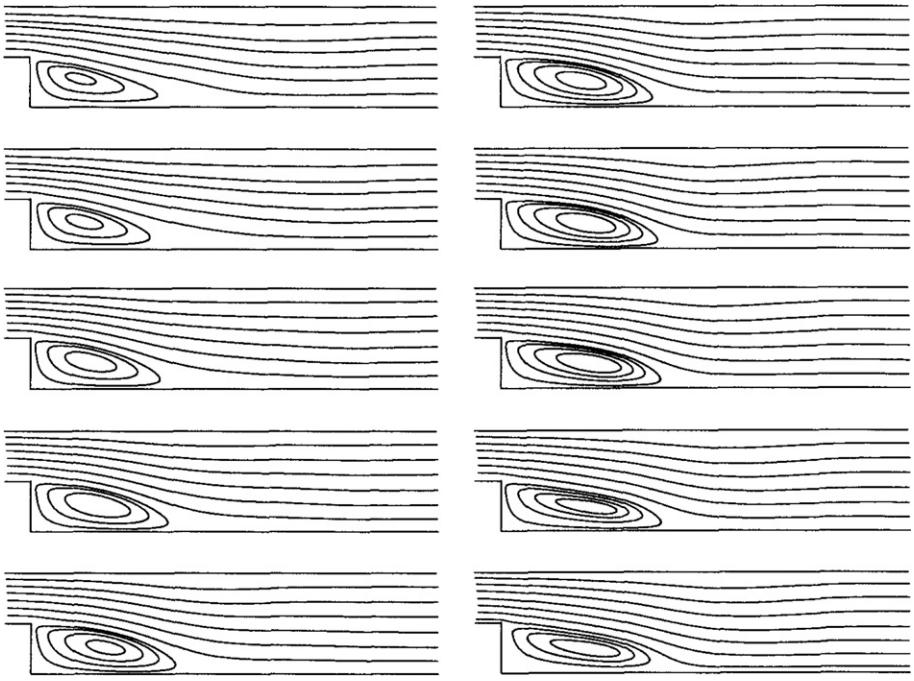

Fig. 13. Snapshots of the streamlines for case 13 along a pulsating cycle. Time reads top-bottom left-right. Snapshots are equally spaced in time.

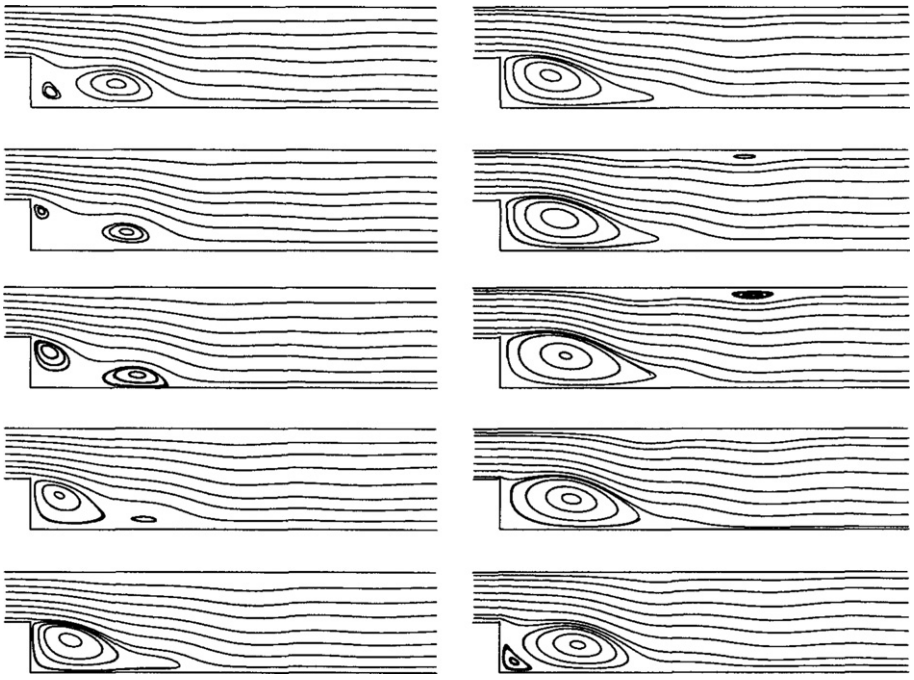

Fig. 14. Snapshots of the streamlines for case 37 along a pulsating cycle. Time reads top-bottom left-right. Snapshots are equally spaced in time.

An overview of three snapshots of the temperature field associated with case 33 is shown in Fig. 15. These temperature snapshots (the dark grey shade signals the highest temperature) correspond to the second, fifth and eighth sub-plots of Fig. 11, respectively. In the two lower sub-plots, it is possible to see how the large vortex located downstream of the step entrains hot fluid from the wall region and how, when the vortex disappears, the hot fluid is convected away (see upper plot).

Finally, a comment should be made on the commonality that exists between the results obtained in this paper and the results reported by other researchers in the turbulent flow regime. Yoshioka et al. [20] have studied the turbulent flow topology behind a back-step when the

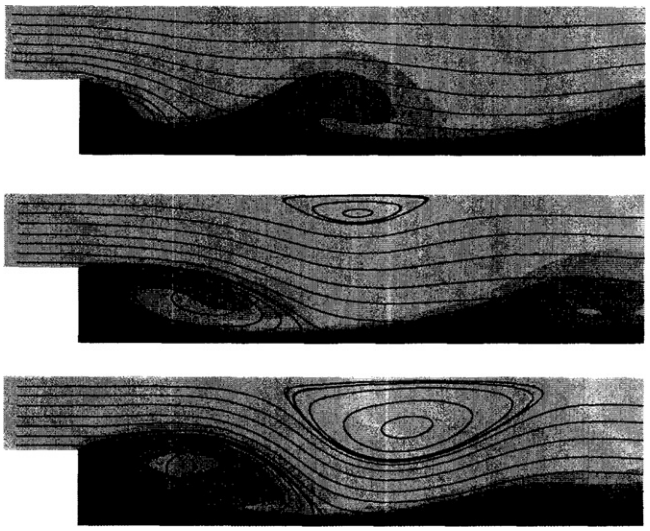

Fig. 15. Temperature snapshots of case 33. Time reads top-bottom. Snapshots are equally spaced in time.

incoming flow is subjected to a periodic perturbation. The perturbation consisted on the implementation of an alternating suction/injection (inclined 45° relative to the x-axis) through a slit open right on the step edge. The authors found that the perturbation that has the largest effect on the reattachment length has a Strouhal number (based on the step height and mean inlet velocity) close to 0.2. This value falls approximately within the range reported by other researchers that are referenced in [20]. In our case, we obtain maximum heat transfer enhancement for a Strouhal number (measured by using the same convention as Yoshioka et al. [20] close to 0.1). A factor of 2 exists between those two critical Strouhal numbers, but it should be borne in mind that the problems also have large differences; namely: (a) the Reynolds number in the turbulent flow studies is about 100 times larger than in our case, (b) the nature of the perturbation is very different, and (c) our velocity profile is parabolic right before the step, while it is nearly flat in the turbulent flow studies. Nevertheless, both problems have in common the existence of a critical Strouhal number that markedly affects some fluid dynamics related aspects.

9. Conclusions

The following conclusions could be drawn after the completion of the work:

- It has been found that forced flow pulsation in the inlet duct of a 2-D back step channel modifies substantially flow topology in the low Reynolds number regime. In particular, instead of a single recirculation bubble anchored to the step, several separated flow regions appear and disappear periodically as the pulsating cycles proceed. Some of the separated flow regions appear in the upper wall of the channel. The recirculation region behind the step undergoes a dynamic process in which a single vortex expands, breaks into a pair of vortices, contracts, and expands again. This dynamic behaviour is controlled by two parameters: frequency of the velocity pulsation and amplitude of the oscillating pressure gradient at the inlet section.
- These periodic changes in the flow topology enhance convective mixing and, accordingly, increase the local Nusselt number in the region located right behind the step. We have computed the Nusselt number in a horizontal region whose length is four times the step height at Reynolds 100, and found that the time-averaged Nusselt number could become 55% larger than in the steady-state case. This heat transfer enhancement is the maximum that could be obtained without having flow reversal at either the inlet or outlet flow sections.
- This Nusselt number enhancement appears to be of a resonant nature. For a given inlet pressure gradient amplitude, its reaches it maximum for a specific pulsating frequency and decreases for both higher and lower values of the frequency. For a given frequency, the Nusselt number is higher the larger is the inlet pressure gradient amplitude.
- We found that heat transfer enhancement is larger when it is assumed that water has temperature dependent viscosity and thermal conductivity. The reason could be that local Reynolds numbers in the vicinity of the heated wall are larger when considering this real fluid behaviour.
- The behaviour that has been described in the previous paragraph suggests that it might be feasible to exert some kind of flow control by forcing unsteady behaviour on a reference steady regime. This, of course, might not happen for any type of flow; indeed, published data seems to point out that flow pulsation in straight channels does not influence the time-averaged Nusselt number. That is: the existence of resonant effects may require the presence of a suitable geometric configuration. In this context, it is worth to note that, at Reynolds 100, the resonant frequency $\omega = 0.15$ is close to the typical vortex shedding Strouhal number (of the order of 0.15–0.20, depending on the blockage ratio) associated with the flow around a square cylinder.

Acknowledgements

This work has been funded by the Spanish Ministry of Science and Education (Ministerio de Investigation y Ciencia) under PROFIT contract: CIT-020400-2005-4. The authors gratefully acknowledge this support.

References

[1] B.F. Armaly, F. Durst, J. Pereira, Experimental and theoretical investigation of backwards facing step flow, J. Fluid Mech. 127 (1983) 473–496.

[2] F. Durst, J.C.F. Pereira, Time dependent laminar backward facing step flow in a two dimensional duct, J. Fluid Eng. 110 (1988) 289–296.

[3] L. Kaiktsis, G.E. Kairnaidakis, S.A. Orszag, Onset of three dimensionality, equilibria, and early transition in flow over a backward facing step, J. Fluid Mech. 231 (1991) 501–558.
[4] D. Barkley, M.G. Gomes, R. Henderson, Three dimensional instability in flow over a backward facing step, J. Fluid Mech. 473 (2002) 167–190.
[5] F.P. Incropera, D.P. DeWitt, Introduction to Heat Transfer, John Wiley & Sons, 1996, table A-6, p. 764.
[6] J.C. Yu, Z.X. Li, T.S. Zhao, An analytical study of pulsating laminar heat convection in a circular tube with constant heat flux, Int. J. Heat Mass Transfer 47 (2004) 5297–5301.
[7] M. Faghri, K. Javadani, A. Faghri, Heat transfer with laminar pulsating flow in a pipe, Lett. Heat Mass Transfer 6 (1979) 259–270.
[8] H.N. Hemida, M.N. Sabry, A. Abdel-Rahim, H. Mansour, Theoretical analysis of heat transfer in laminar pulsating flow, Int. J. Heat Mass Transfer 45 (2002) 1767–1780.
[9] M.R. Mackley, P. Stonestreet, Heat transfer and associated energy dissipation for oscillatory flow in baffled tubes, Chem. Sci. Eng. 50 (14) (1995) 2211–2224.
[10] T. Moschandreu, M. Zamir, Heat transfer in a tube with pulsating flow and constant heat flux, Int. J. Heat Mass Transfer 40 (1997) 2461–2466.
[11] H. Chattopadhyay, F. Durst, S. Ray, Analysis of heat transfer in simultaneously developing pulsating laminar flow in a pipe with constant wall temperature, Int. Commun. Heat Mass Transfer 33 (2006) 475–481.
[12] H.I. Abu-Malaweh, A review of research on laminar mixed convection flow over a backward and forward facing steps, Int. J. Therm. Sci. 42 (2003) 897–909.
[13] B. Abu-Hijleh, Heat transfer from a 2D backward facing sep with isotropic porous floor segments, Int. J. Heat Mass Transfer 43 (2000) 2727–2737.
[14] J.H. Nie, B.F. Armaly, Three dimensional convective flow adjacent to backward facing step, effects of step height, Int. J. Heat Mass Transfer 45 (2002) 2431–2438.
[15] H. Iwai, K. Nakabe, K. Suzuki, Flow and heat transfer characteristics of backward-facing step laminar flow in a rectangular duct, Int. J. Heat Mass Transfer 43 (2000) 57–471.
[16] T.P. Chiang, T.W.H. Sheu, A numerical revisit of backward facing step flow problem, Phys. Fluid 11 (1999) 862–874.
[17] A. Valencia, L. Hinojosa, Numerical solutions of pulsating flow and heat transfer characteristics in a channel with a backward-facing step, Heat Mass Transfer 32 (1997) 143–148.
[18] A. Valencia, Effect of pulsating inlet on the turbulent flow and heat transfer past a backward-facing step, Int. Commun. Heat Mass Transfer 24 (1997) 1009–1018.
[19] Y.M. Chang, P.G. Tucker, Numerical studies of heat transfer enhancements in laminar separated flows, Int. J. Heat Fluid Flow 25 (2004) 22–31.
[20] S. Yoshioka, S. Obi, S. Masuda, Organised vortex motion in periodically perturbed turbulent separated flow over a backward-facing step, Int. J. Heat Fluid Flow 22 (2001) 301–307.
[21] D. Das, J.H. Arakeri, Transition of unsteady velocity profiles with reverse flow, J. Fluid Mech. 374 (1998) 251–283.
[22] R. Akhavan, R.D. Kamm, A.H. Shapiro, An investigation of transition to turbulence in bounded oscillatory Stokes flows, Part 1: experiments, J. Fluid Mech. 225 (1991) 395–422.
[23] R. Akhavan, R.D. Kamm, A.H. Shapiro, An investigation of transition to turbulence in bounded oscillatory Stokes flows, Part 2: numerical simulations, J. Fluid Mech. 225 (1991) 423–444.
[24] M. Hino, M. Sawamoto, S. Takasu, Experiments on transition to turbulence in an oscillatory pipe flow, J. Fluid Mech. 75 (1976) 193–207.
[25] R.L. Panton, Incompressible Flow, John Wiley, New York, 1996.
[26] M.A. Olshanskii, V.M. Staroverov, On simulation of outflow boundary conditions in finite difference calculations for incompressible fluid, Int. J. Numer. Meth. Fluid 33 (2000) 499–534.
[27] N. Hasan, S.F. Anwer, S. Sanghi, On the outflow boundary condition for external incompressible flows: a new approach, J. Comput. Phys. 206 (2005) 661–683.
[28] J. Nordstrom, K. Mattsson, C. Swanson, Boundary conditions for a divergence free velocity–pressure formulation of the Navier–Stokes equations, J. Comput. Phys. 225 (2007) 874–890.
[29] L. Kaiktsis, G. Karniadakis, S.A. Orszag, Unsteadyness and convective instabilities in two-dimensional flow over a backward facing step, J. Fluid Mech. 321 (1996) 157–187.
[30] X. Wang, N. Zhang, Numerical analysis of heat transfer in pulsating turbulent flow in a pipe, Int. J. Heat Mass Transfer 48 (2005) 3957–3970.
[31] M. Wang, T. Sheu, Implementation of a free boundary condition to Navier–Stokes equations, Int. J. Numer. Meth. Heat Fluid Flow 7 (1997) 11–95.
[32] B. Mendez, A. Velazquez, Finite Point Solver for the simulation of 2-D laminar incompressible unsteady flows, Comput. Meth. Appl. Mech. Eng. 193 (2004) 825–848.
[33] B. Mendez, A. Velazquez, Finite Point based numerical study on the unsteady laminar wake behind square cylinders, Int. J. Numer. Meth. Heat Fluid Flow 17 (2007) 108–132.
[34] J.C. Tannehill, D.A. Anderson, R.H. Fletcher, Computational Fluid Mechanics and Heat Transfer, Taylor & Francis, Philadelphia, 1997.
[35] C. Kiris, D. Kwak, Aspects of unsteady incompressible flow simulations, Comput. Fluids 31 (2002) 627–638.
[36] R. Peyret, Unsteady evolution of a horizontal jet in a stratified fluid, J. Fluid Mech. 78 (1976) 49–63.
[37] T. Nishimura, N. Oka, Y. Yoshinaka, K. Kunitsugu, Influence of imposed oscillatory frequency on mass transfer enhancement of grooved channels for pulsatile flow, Int. J. Heat Mass Transfer 43 (2000) 2365–2374.
[38] M. Greiner, P.F. Fischer, H.M. Tufo, Two dimensional simulations of enhanced heat transfer in an intermittently grooved channel, J. Heat Transfer 124 (2002) 538–545.
[39] M. Greiner, P.F. Fischer, H. Tufo, Numerical simulations of resonant heat transfer augmentation at low Reynolds numbers, J. Heat Transfer 124 (2002) 1169–1175.